Supplement of Aerosol Research, 4, 603–623, 2026
https://doi.org/10.5194/ar-4-603-2026-supplement
© Author(s) 2026. CC BY 4.0 License.



AEROSOL Research
Open Access

Supplement of

Contributions of fine and coarse particles to light absorption at an urban traffic site during street dust season

Luis M. F. Barreira et al.

Correspondence to: Luis M. F. Barreira (luis.barreira@fmi.fi)

The copyright of individual parts of the supplement might differ from the article licence.

S1 – Supplemental tables and graphics

Table S1: Pearson correlation coefficients (r) between light absorption coefficients in $PM_{2.5-7.2}$ at different wavelengths and the fractional contributions of PMF-derived source factors in $PM_{2.5-10}$. Each fractional contribution was calculated by dividing the source-factor concentration by the sum of the concentrations of the five source factors. Source factors include dust, non-exhaust emissions (NEE), combustion/secondary inorganic aerosol (Comb/SIA), fresh salt, and aged salt.

	$b_{370\ nm}$	$b_{470\ nm}$	$b_{520\ nm}$	$b_{590\ nm}$	$b_{660\ nm}$	$b_{880\ nm}$	$b_{950\ nm}$	Dust	Comb/ SIA	NEE	Salt (fresh)	Salt (aged)
$b_{370\ nm}$	1.00	0.98	0.97	0.95	0.95	0.92	0.92	0.39	-0.16	-0.27	-0.27	-0.22
$b_{470\ nm}$	0.98	1.00	1.00	0.99	0.99	0.97	0.97	0.43	-0.18	-0.30	-0.29	-0.26
$b_{520\ nm}$	0.97	1.00	1.00	1.00	0.99	0.98	0.98	0.43	-0.19	-0.28	-0.30	-0.26
$b_{590\ nm}$	0.95	0.99	1.00	1.00	1.00	0.99	0.99	0.44	-0.18	-0.29	-0.30	-0.27
$b_{660\ nm}$	0.95	0.99	0.99	1.00	1.00	0.99	0.99	0.45	-0.19	-0.29	-0.32	-0.28
$b_{880\ nm}$	0.92	0.97	0.98	0.99	0.99	1.00	1.00	0.46	-0.20	-0.26	-0.33	-0.30
$b_{950\ nm}$	0.92	0.97	0.98	0.99	0.99	1.00	1.00	0.47	-0.19	-0.28	-0.34	-0.30
Dust	0.39	0.43	0.43	0.44	0.45	0.46	0.47	1.00	-0.21	-0.60	-0.68	-0.71
Comb/ SIA	-0.16	-0.18	-0.19	-0.18	-0.19	-0.20	-0.19	-0.21	1.00	-0.30	0.30	0.18
NEE	-0.27	-0.30	-0.28	-0.29	-0.29	-0.26	-0.28	-0.60	-0.30	1.00	0.06	0.37
Salt (fresh)	-0.27	-0.29	-0.30	-0.30	-0.32	-0.33	-0.34	-0.68	0.30	0.06	1.00	0.10
Salt (aged)	-0.22	-0.26	-0.26	-0.27	-0.28	-0.30	-0.30	-0.71	0.18	0.37	0.10	1.00

Table S2: Model fit statistics for the multiple linear regression models at 370, 520, and 660 nm. R and R^2 values are reported for each wavelength.

	R	R^2
370 nm	0.866	0.751
520 nm	0.919	0.844
660 nm	0.937	0.878

Table S3: Multiple linear regression coefficients for the elemental predictors of light absorption at 370, 520, and 660 nm. Estimates, standard errors (SE), t-statistics, and p-values are shown for each predictor.

Predictor	Estimate	SE	t	p
370 nm				
Intercept	-0.08	0.35	-0.23	0.823
Al	2.07	0.41	5.02	<0.001
Cu	-87.61	38.79	-2.26	0.031
S	5.69	5.29	1.08	0.289
Na	2.28	2.71	0.84	0.407
Cl	-0.09	0.97	-0.09	0.927
520 nm				
Intercept	-0.19	0.19	-0.99	0.328
Al	1.31	0.23	5.71	<0.001
Cu	-17.57	21.58	-0.81	0.421
S	3.17	2.94	1.08	0.290
Na	1.25	1.51	0.83	0.414
Cl	-0.08	0.54	-0.15	0.880
660 nm				
Intercept	-0.15	0.14	-1.11	0.274
Al	1.06	0.16	6.55	<0.001
Cu	-2.22	15.22	-0.15	0.885
S	2.69	2.07	1.30	0.204
Na	0.40	1.06	0.38	0.709
Cl	0.04	0.38	0.11	0.912

Table S4: Collinearity diagnostics for the predictors included in the multiple linear regression models. Variance inflation factor (VIF) and tolerance values are reported for each predictor.

	VIF	Tolerance
Al	4.40	0.227
Cu	3.55	0.282
S	1.30	0.769
Na	10.19	0.098
Cl	5.28	0.190

Table S5: Pearson correlation matrix showing the pairwise correlations among eBC in $PM_{2.5-7.2}$ and elemental species (Al, Cu, S, Na, and Cl) measured in $PM_{2.5-10}$.

	eBC	Al	Cu	S	Na	Cl
eBC	1.00	0.94	0.81	0.45	0.73	0.41
Al	0.94	1.00	0.82	0.39	0.74	0.39
Cu	0.81	0.82	1.00	0.41	0.71	0.39
S	0.45	0.39	0.41	1.00	0.44	0.38
Na	0.73	0.74	0.71	0.44	1.00	0.83
Cl	0.41	0.39	0.39	0.38	0.83	1.00

Table S6: Pearson correlation matrix showing the pairwise correlations among eBC in $PM_{2.5-7.2}$ and the absolute concentrations of PMF-derived source factors in $PM_{2.5-10}$: du All instruments sampled PM_1 during the intercomparison, with the MAAP used for comparison st, combustion/secondary inorganic aerosol (Comb/SIA), non-exhaust emissions (NEE), fresh salt, and aged salt.

	eBC	Dust	Comb/SIA	NEE	Salt (fresh)	Salt (aged)
eBC	1.00	0.94	0.33	0.88	0.42	0.25
Dust	0.94	1.00	0.30	0.89	0.40	0.27
Comb/SIA	0.33	0.30	1.00	0.26	0.45	-0.08
NEE	0.88	0.89	0.26	1.00	0.30	0.27
Salt (fresh)	0.42	0.40	0.45	0.30	1.00	0.02
Salt (aged)	0.25	0.27	-0.08	0.27	0.02	1.00

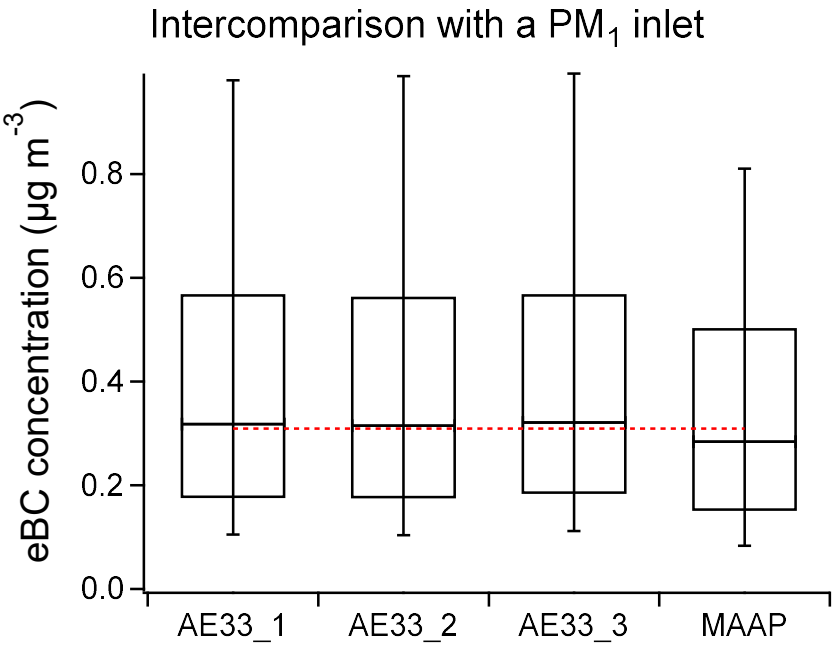


Figure S1: Intercomparison of equivalent black carbon (eBC) concentrations measured by three AE33 aethalometers and a MAAP. All instruments sampled PM_1 during the intercomparison, with the MAAP used for comparison. During the main campaign, AE33_1, AE33_2, and AE33_3 measured PM_1, $PM_{2.5}$, and $PM_{7.2}$, respectively. The mean eBC concentration across all instruments is indicated by the red dotted line.

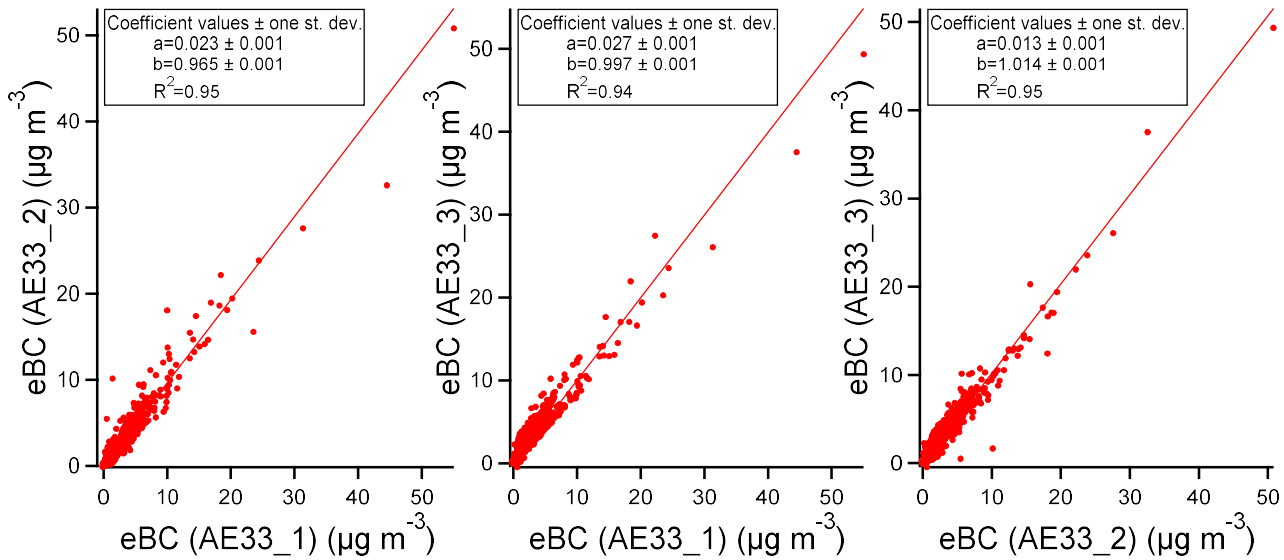


Figure S2: Pairwise comparison of equivalent black carbon (eBC) concentrations measured in PM1 by three AE33 instruments (AE33_1, AE33_2, and AE33_3), used to measure light absorption in PM_1, $PM_{2.5}$, and $PM_{7.2}$, respectively. Scatter plots show eBC from AE33_2 versus AE33_1, AE33_3 versus AE33_1, and AE33_3 versus AE33_2.

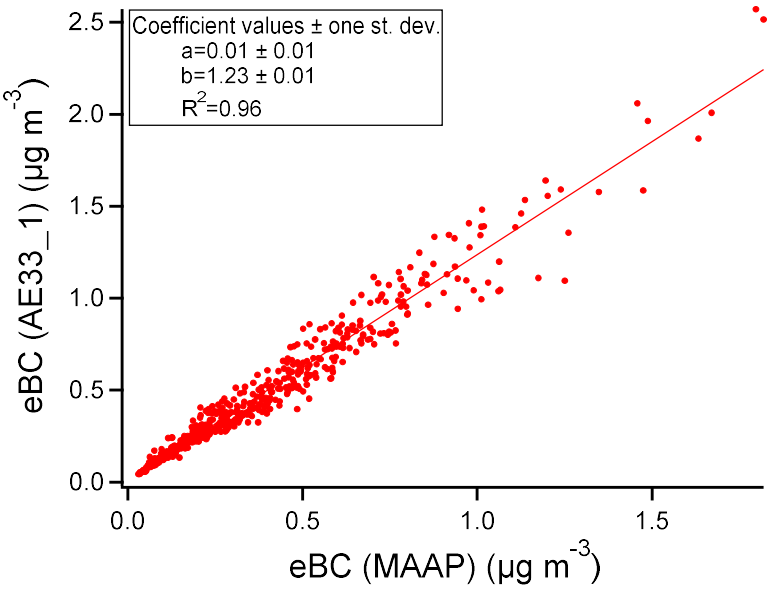


Figure S3: Comparison of hourly-averaged equivalent black carbon (eBC) concentrations measured in PM_1 by the AE33 aethalometer (AE33_1) and MAAP.

40

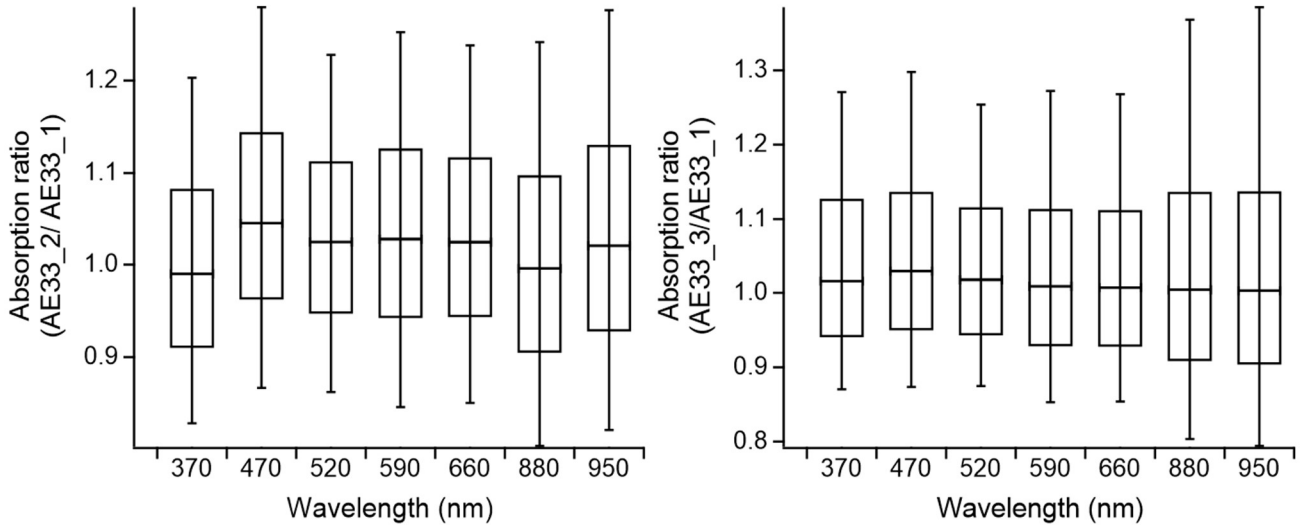


Figure S4: Ratios of light absorption measured during the intercomparison, when all three AE33 instruments sampled PM_1. The left panel shows the absorption ratio of AE33_2 to AE33_1, while the right panel shows the ratio of AE33_3 to AE33_1.

45

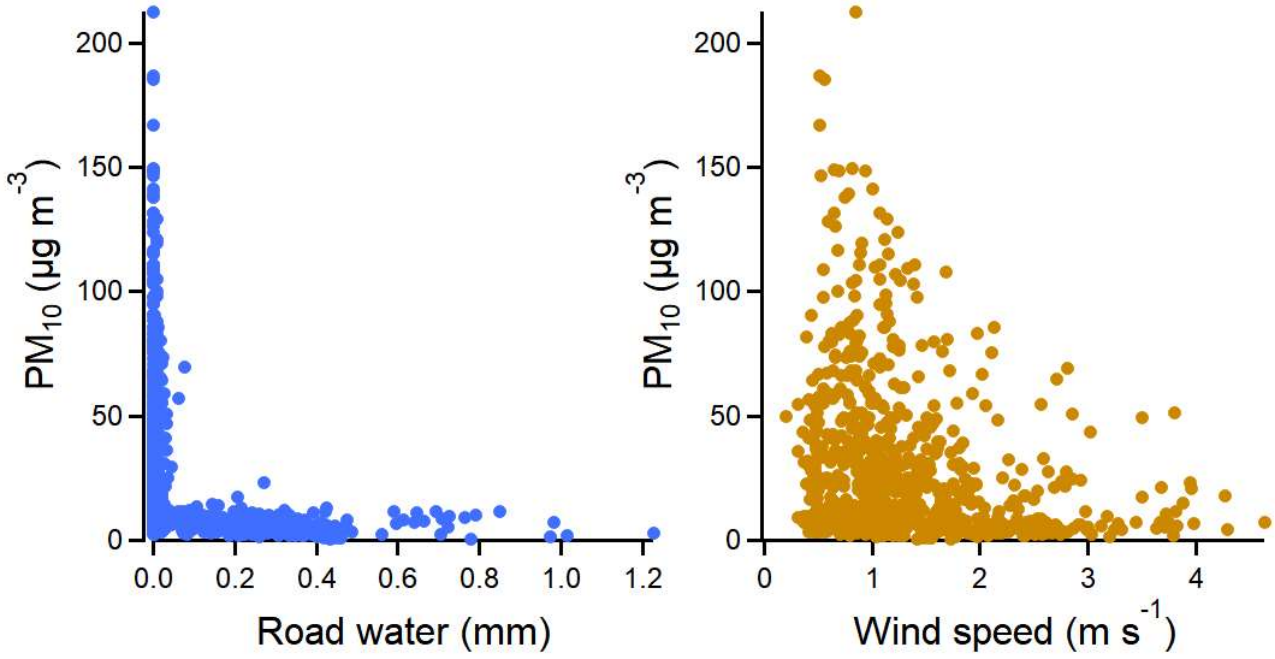


Figure S5: Scatter plots of PM_{10} mass concentration as a function of road surface wetness (left) and wind speed (right) during the measurement campaign.

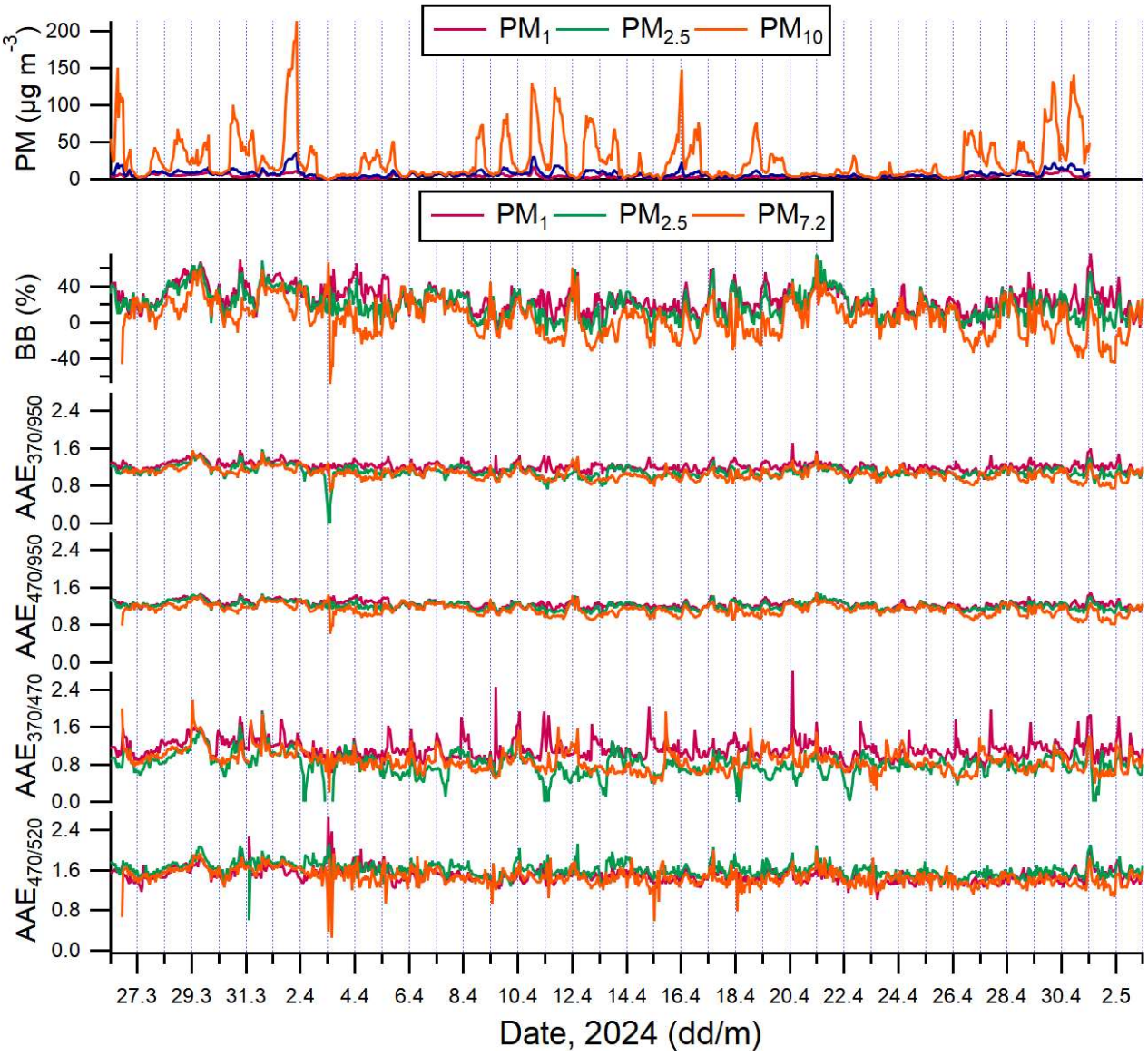


Figure S6: Time series of the Absorption Ångström Exponent (AAE), calculated for different wavelength pairs (370/470, 470/950, 370/950, and 470/520 nm), and of BB percentage in PM_1 (brown), $PM_{2.5}$ (blue), and $PM_{7.2}$ (orange) during the measurement campaign. For comparison, the top panel shows the total PM mass concentration for PM_1, $PM_{2.5}$, and PM_{10}, using the same colour scheme.

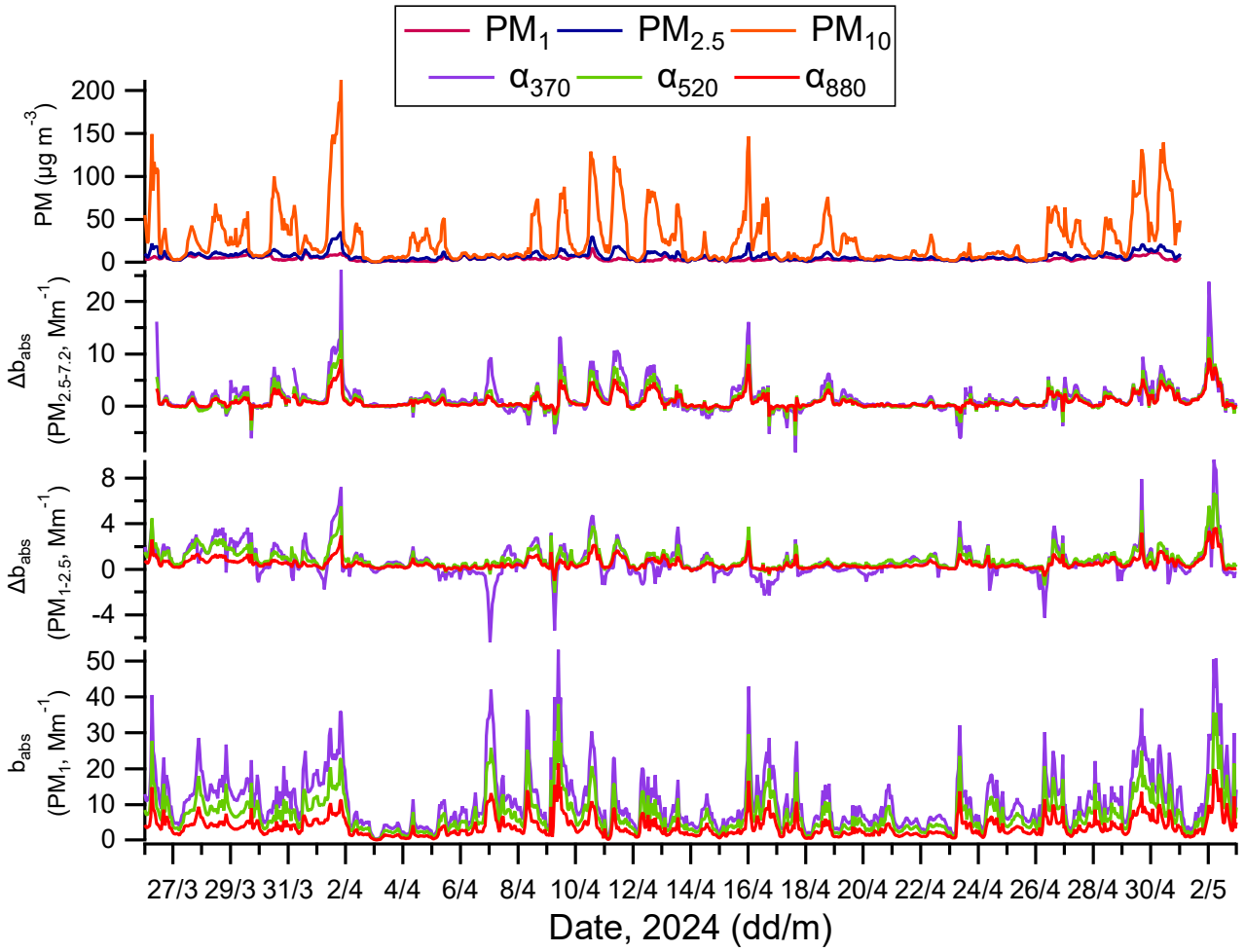


Figure S7: Time series of hourly mean absorption coefficients for different PM size fractions (the stacked panels show PM_1 at the bottom, $PM_{1\text{-}2.5}$ in the middle lower panel, and $PM_{2.5\text{-}7.2}$ in the upper lower panel; purple = 370 nm, green = 520 nm, and red = 880 nm). For comparison, the top panel shows hourly mean total PM mass concentration in PM_1 (brown), $PM_{2.5}$ (blue), and PM_{10} (orange).

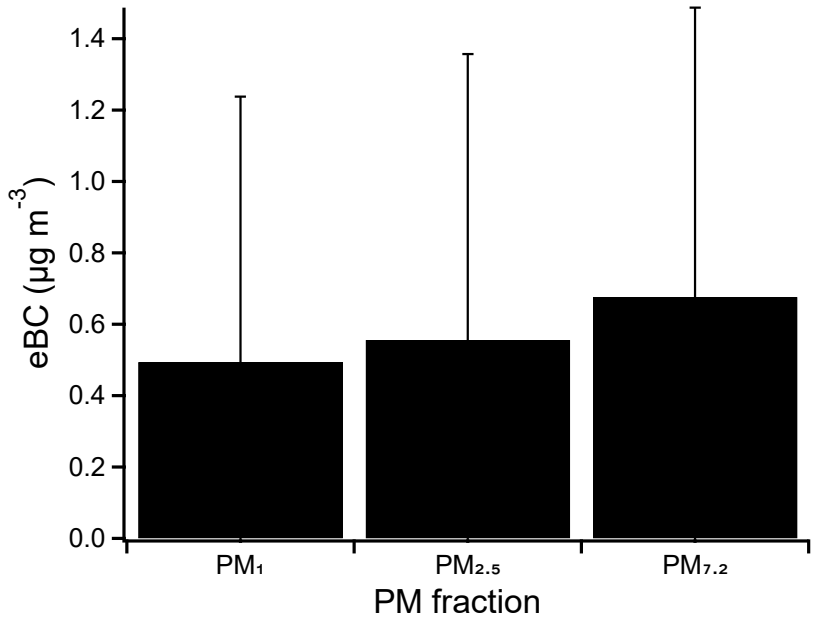


Figure S8: Campaign-averaged concentrations and standard deviations of equivalent black carbon (eBC) in PM_1, $PM_{2.5}$, and $PM_{7.2}$ fractions (expressed in µg m^{-3}).

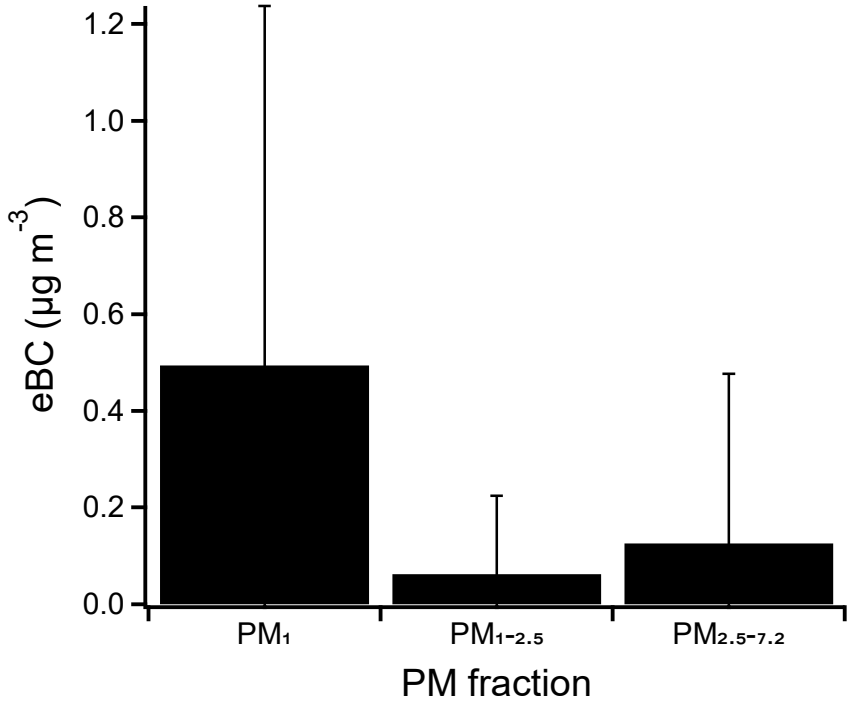


Figure S9: Campaign-averaged concentrations of equivalent black carbon (eBC) in the PM_1, $PM_{1\text{-}2.5}$, and $PM_{2.5\text{-}7.2}$ fractions (expressed in µg m^{-3}).

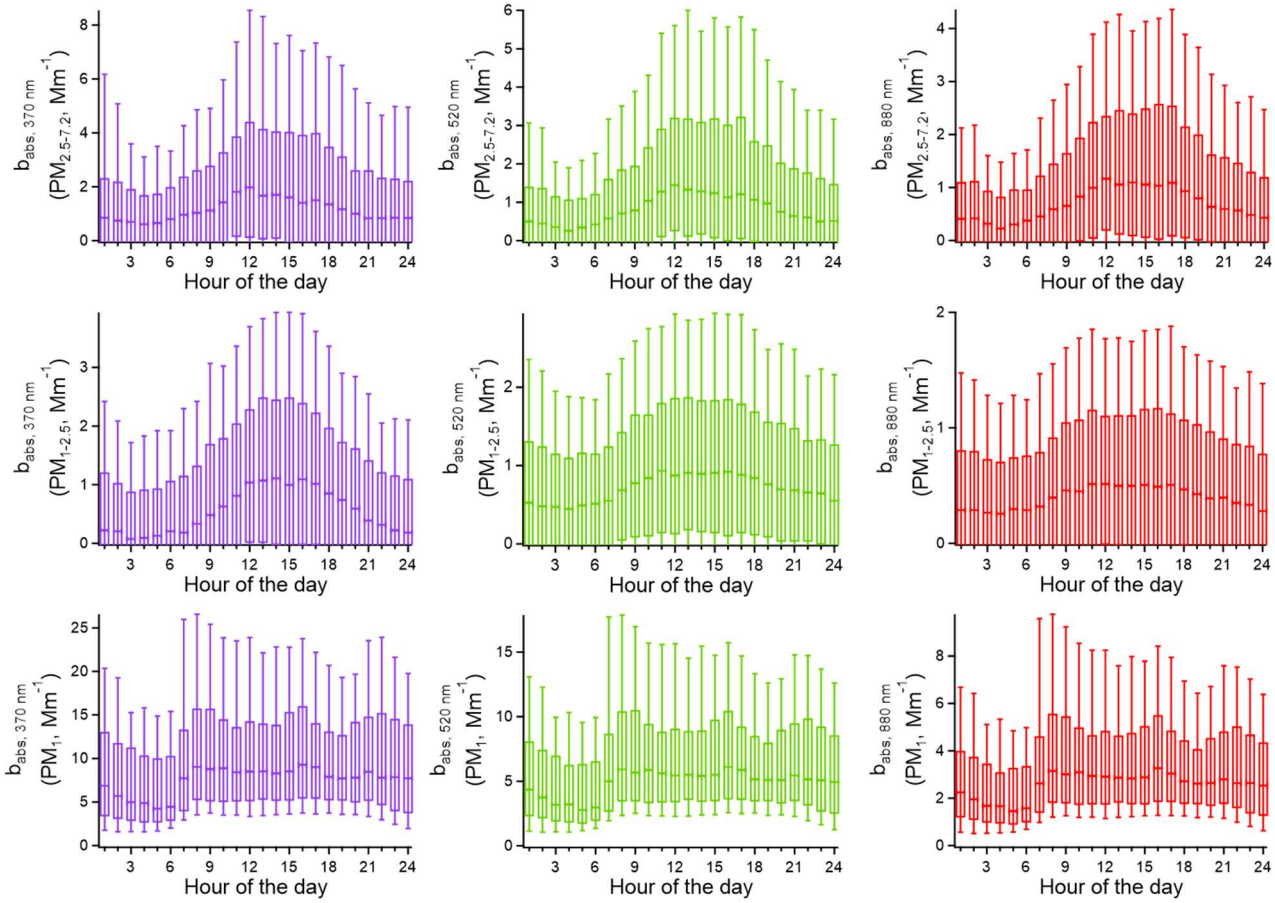


Figure S10: Diurnal variation of absorption coefficients for different particle size fractions. Panels show absorption in PM_1 (bottom), $PM_{1\text{-}2.5}$ (middle), and $PM_{2.5\text{-}7.2}$ (top) at 370 nm (purple), 520 nm (green), and 880 nm (red). In each box, the mid-line represents the median, box edges indicate the 25th and 75th percentiles, and whiskers extend from the 10th to 90th percentiles. The y-axis was set to zero since absorption differences are inherently positive and, therefore, any small negative values that may occur are due to instrument noise or minor data processing variability which are not physically meaningful.

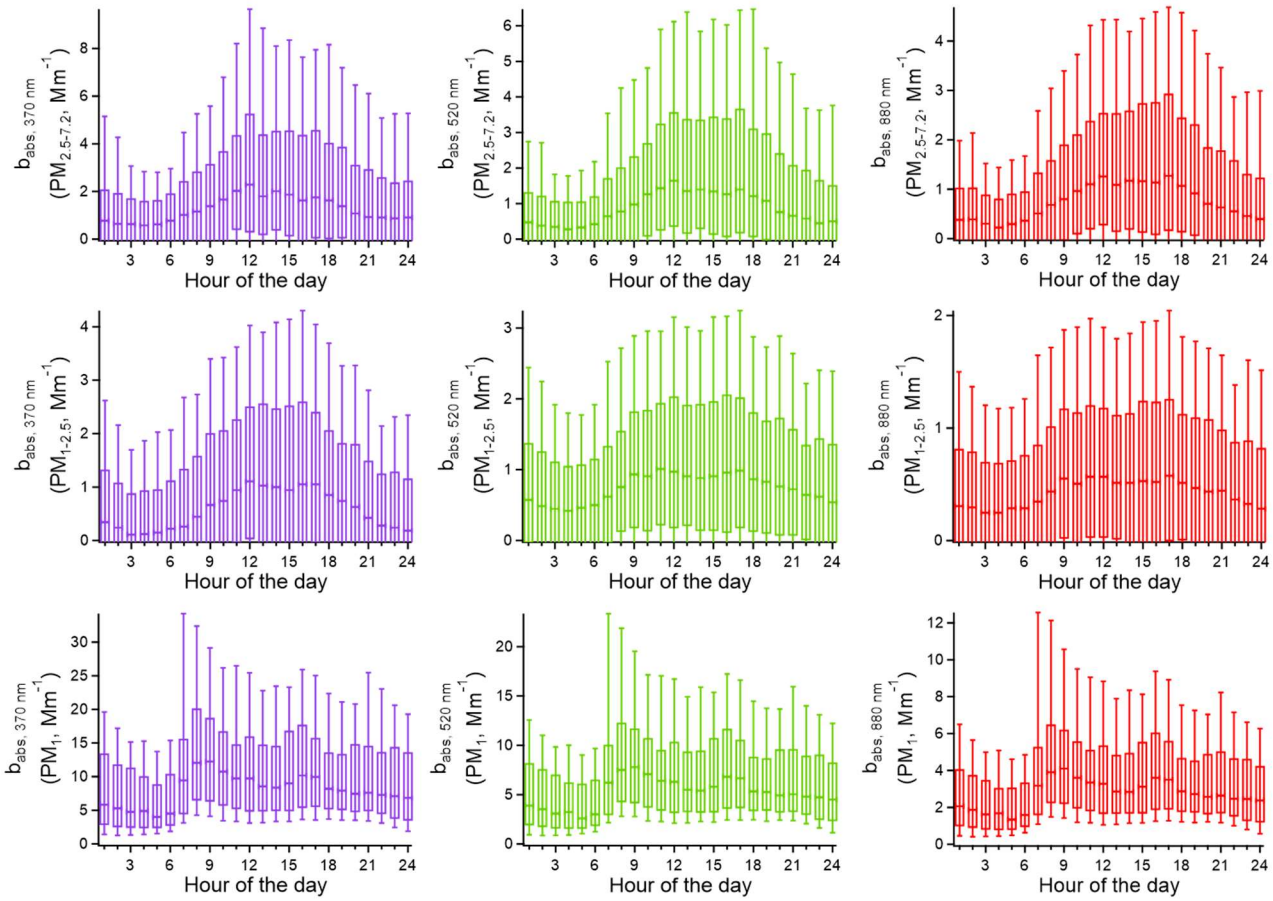


Figure S11: Diurnal variation of absorption coefficients for different particle size fractions during weekdays. Panels show absorption in PM_1 (bottom), $PM_{1-2.5}$ (middle), and $PM_{2.5-7.2}$ (top) at 370 nm (purple), 520 nm (green), and 880 nm (red). In each box, the mid-line represents the median, box edges indicate the 25th and 75th percentiles, and whiskers extend from the 10th to 90th percentiles. The y-axis was set to zero since absorption differences are inherently positive and, therefore, any small negative values that may occur are due to instrument noise or minor data processing variability which are not physically meaningful.

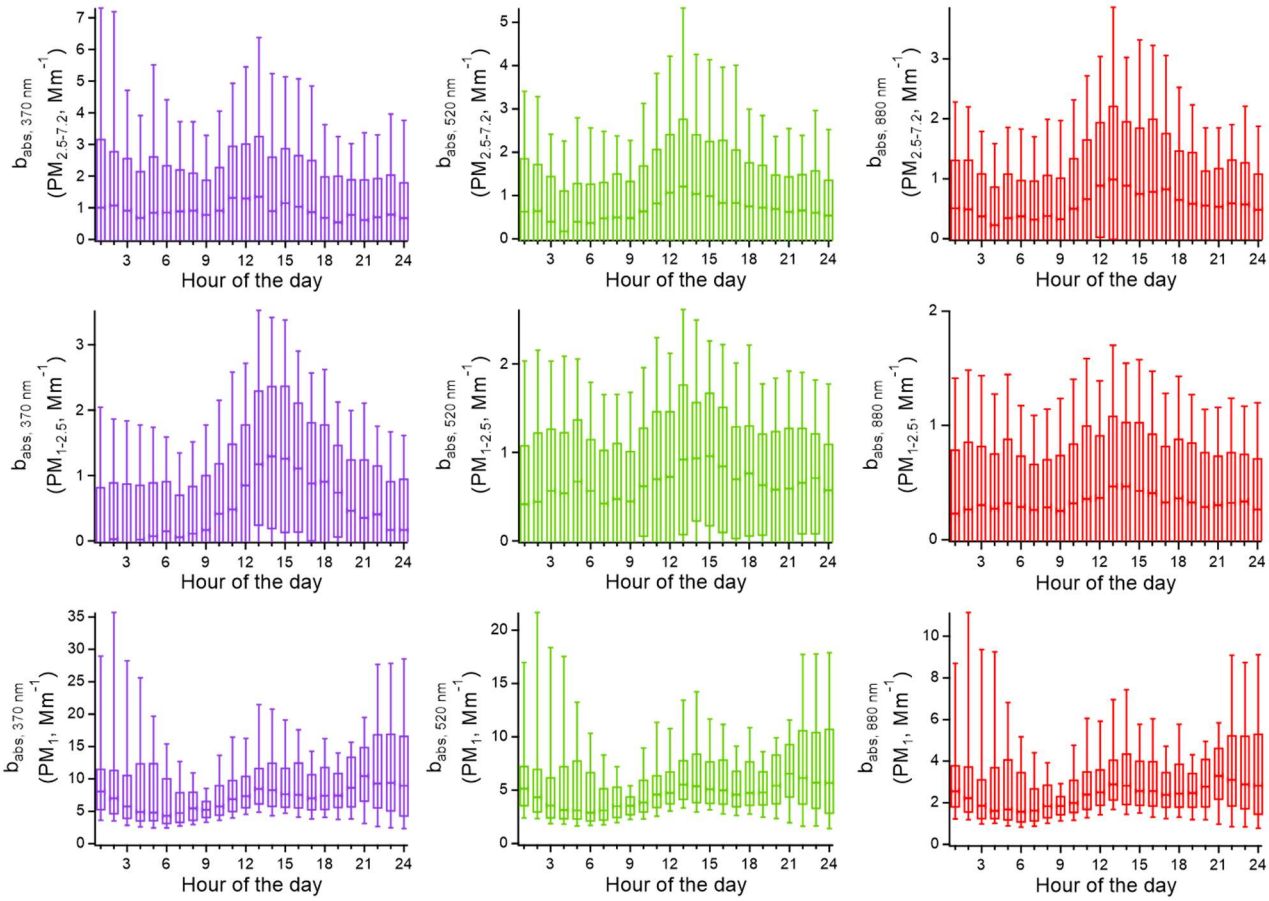


Figure S12: Diurnal variation of absorption coefficients for different particle size fractions during weekends. Panels show absorption in PM_1 (bottom), $PM_{1\text{-}2.5}$ (middle), and $PM_{2.5\text{-}7.2}$ (top) at 370 nm (purple), 520 nm (green), and 880 nm (red). In each box, the mid-line represents the median, box edges indicate the 25th and 75th percentiles, and whiskers extend from the 10th to 90th percentiles. The y-axis was set to zero since absorption differences are inherently positive and, therefore, any small negative values that may occur are due to instrument noise or minor data processing variability which are not physically meaningful.

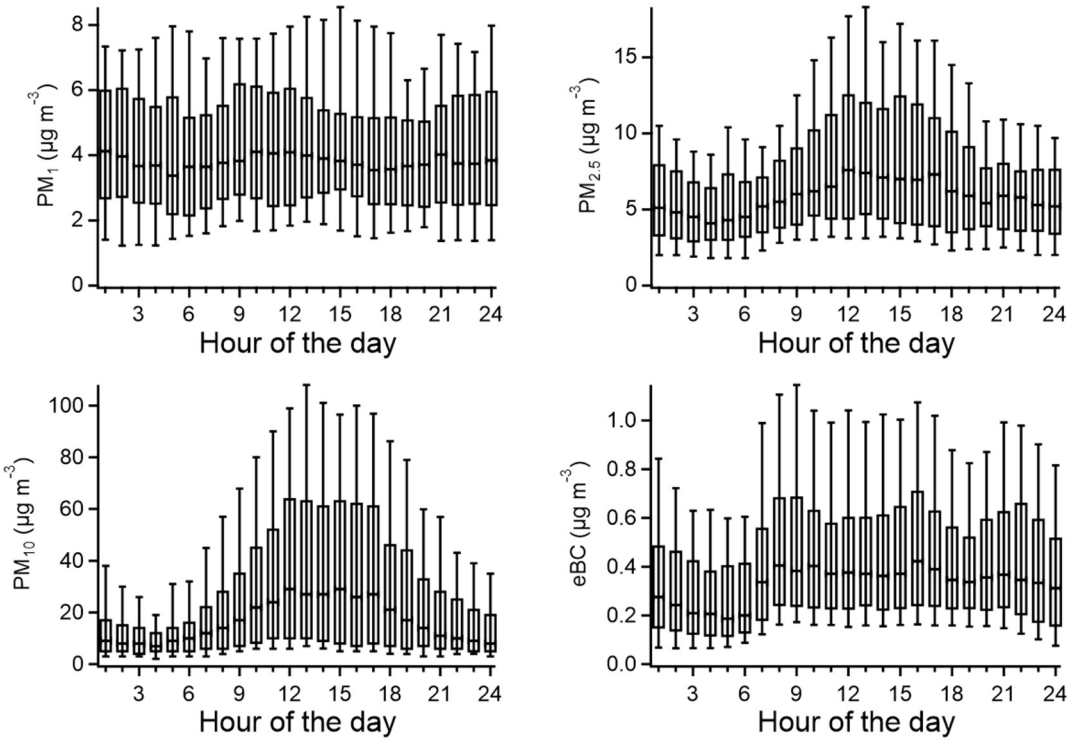


Figure S13: Diurnal variation of particle concentrations: PM_1 (top left), $PM_{2.5}$ (top right), PM_{10} (bottom left), and black carbon in PM_1 (eBC, bottom right). In each box, the mid-line represents the median, the box edges indicate the 25th and 75th percentiles, and whiskers extend from the 10th to 90th percentiles.

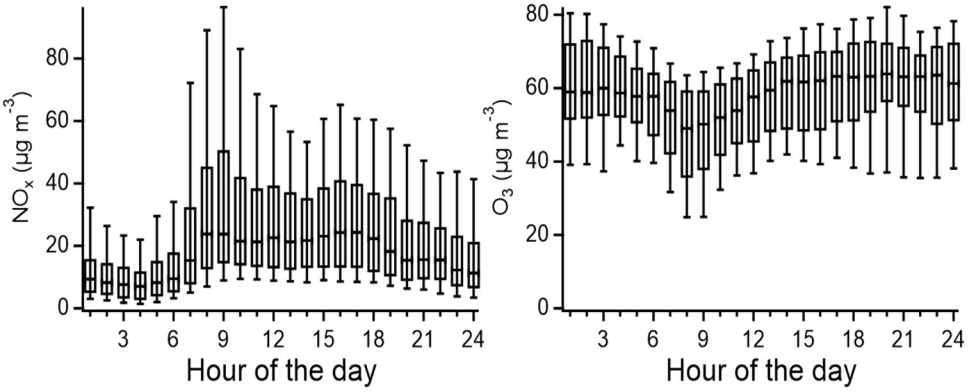


Figure S14: Diurnal variation of NO_X (left) and O_3 (right) concentrations (in µg m^{-3}). In each box, the mid-line represents the median, the box edges indicate the 25th and 75th percentiles, and whiskers extend from the 10th to 90th percentiles.

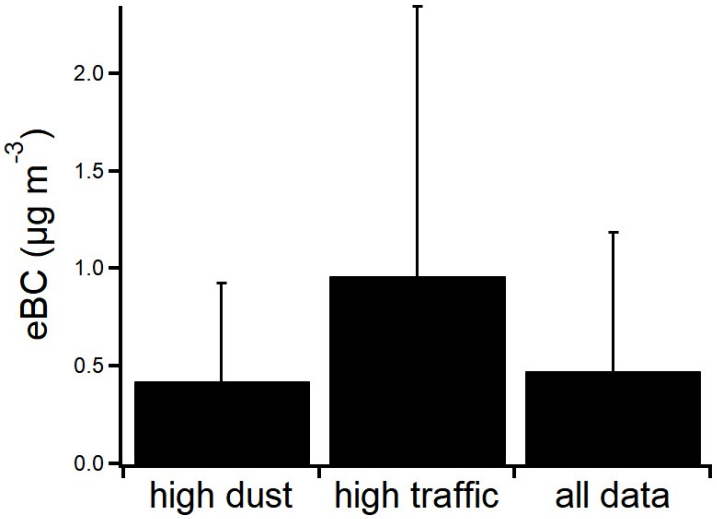
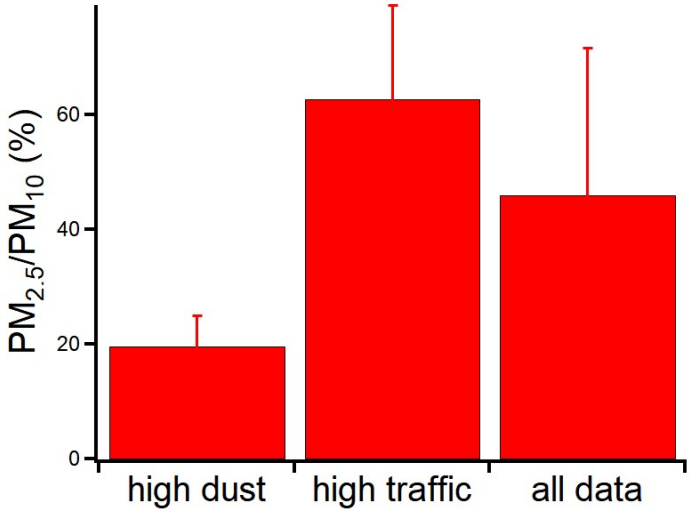
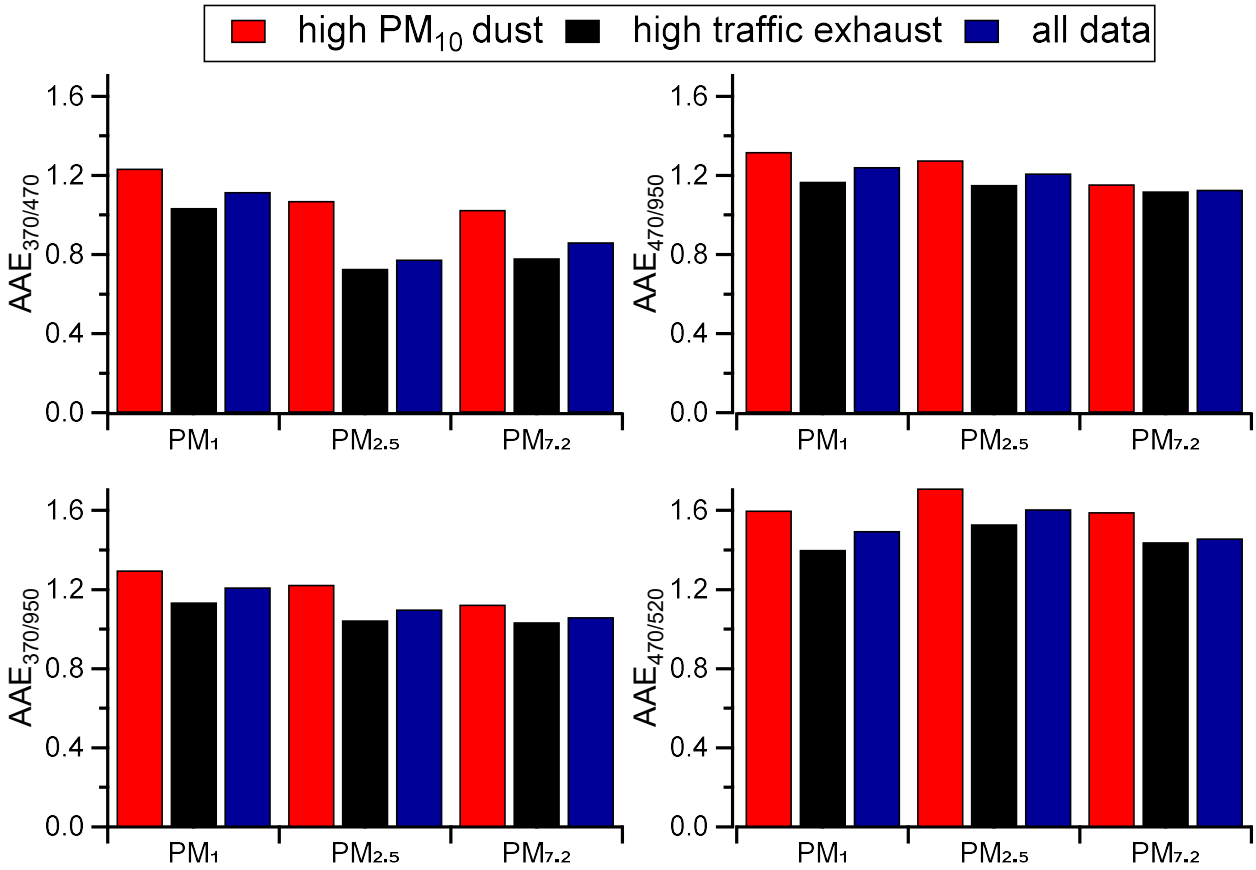


Figure S15: Concentrations of eBC averaged over the entire campaign under different conditions: high PM_{10}: ($PM_{10} \geq 75^{th}$ percentile and $NO_X \leq 50^{th}$ percentile); high traffic: ($PM_{10} \leq 50^{th}$ percentile and $NO_X \geq 75^{th}$ percentile); and all data. The error bars correspond to standard deviations.



100

Figure S16: Mean $PM_{2.5}/PM_{10}$ mass concentration ratio (%) over the entire campaign under different conditions: high PM_{10}: ($PM_{10} \geq 75^{th}$ percentile and $NO_X \leq 50^{th}$ percentile); high traffic: ($PM_{10} \leq 50^{th}$ percentile and $NO_X \geq 75^{th}$ percentile); and all data. The error bars correspond to standard deviations.



105

Figure S17: Absorption Ångström Exponent (AAE) values calculated for wavelength pairs $AAE_{370/470}$, $AAE_{470/950}$, $AAE_{370/950}$, and $AAE_{470/520}$ for PM_1, $PM_{2.5}$, and $PM_{7.2}$ under different pollution conditions: high PM_{10} dust episodes (red; $PM_{10} \geq 75^{th}$ percentile and $NO_x \leq 50^{th}$ percentile), high traffic exhaust conditions (black; $PM_{10} \leq 50^{th}$ percentile and $NO_x \geq 75^{th}$ percentile), and all data combined (blue).

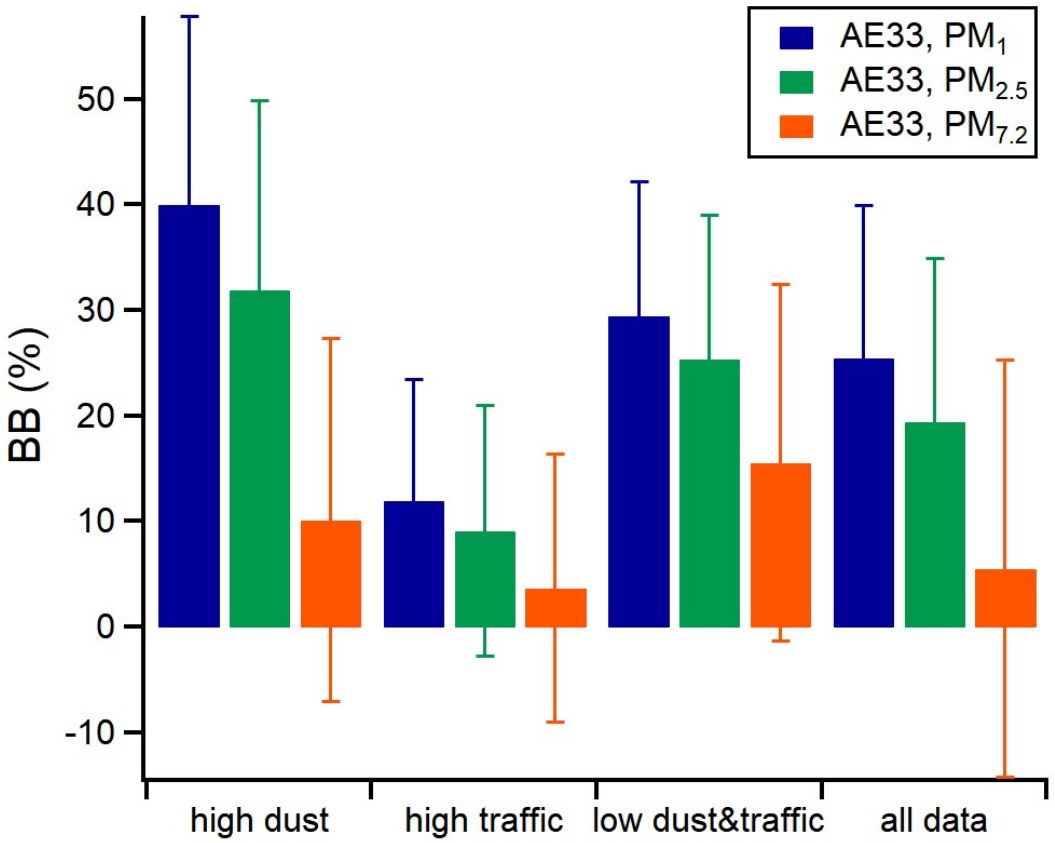


Figure S18: Hourly averaged BB (%) calculated for PM_1 (blue), $PM_{2.5}$ (green), and $PM_{7.2}$ (orange) under different pollution conditions: high PM_{10} dust episodes ($PM_{10} \geq 75^{th}$ percentile and $NO_x \leq 50^{th}$ percentile), high traffic exhaust conditions ($PM_{10} \leq 50^{th}$ percentile and $NO_x \geq 75^{th}$ percentile), low-dust and low-traffic conditions ($PM_{10} \leq 50^{th}$ percentile and $NO_x \leq 50^{th}$ percentile), and all data combined.

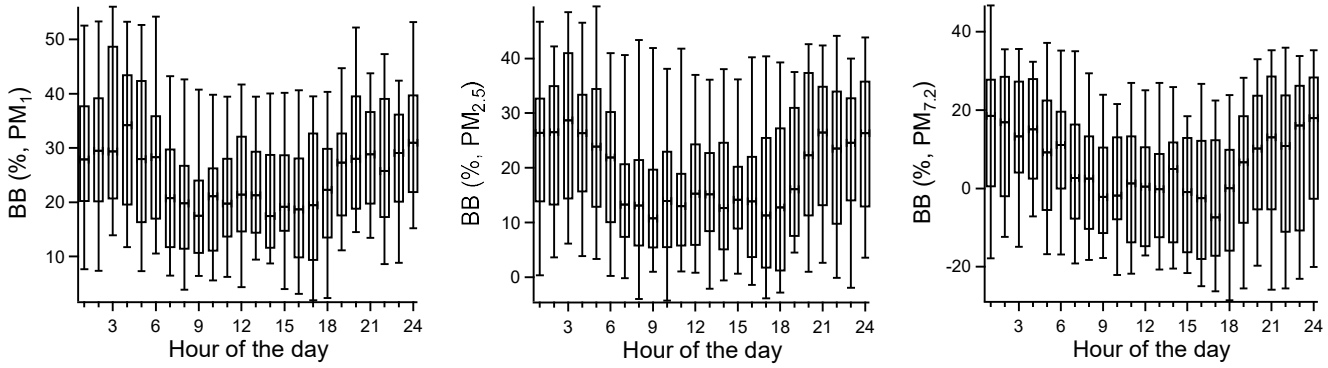
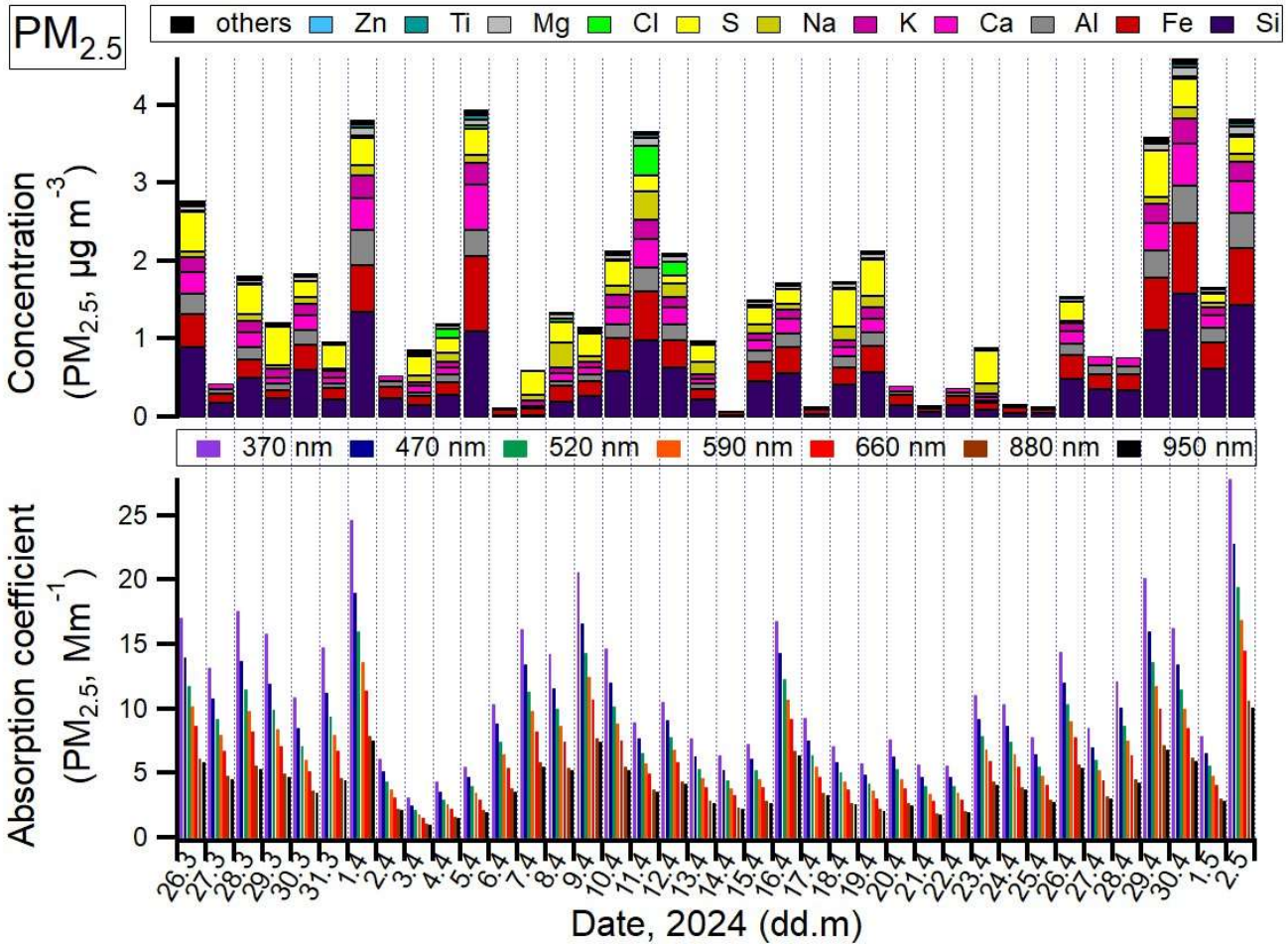


Figure S19: Diurnal variation of BB percentage in PM_1 (left), $PM_{2.5}$ (middle), and $PM_{7.2}$ (right). In each box, the mid-line represents the median, the box edges indicate the 25^{th} and 75^{th} percentiles, and whiskers extend from the 10^{th} to 90^{th} percentiles.



120

Figure S20: Time series of daily-averaged $PM_{2.5}$ absorption coefficients, measured by the AE33 aethalometer at seven wavelengths (bottom panel), and of elemental concentrations in $PM_{2.5}$ obtained from XRF analysis of 24-h filter samples (top panel).

S2 – AE33 measurement uncertainty and incremental absorption

The uncertainty associated with the AE33 absorption measurements was assessed using the intercomparison of the three co-located AE33 instruments. As described in Sect. 2.2.1, the three AE33 instruments sampled PM_1 through the same cyclone under identical sampling conditions during the intercomparison. To estimate the relative uncertainty of each instrument, the coefficient of variation (CV) for each instrument pair was first calculated as Eq. (S1):

$$CV = \frac{SD_{ij}}{(b_i+b_j)/2} \times 100 \quad \text{(S1)}$$

, where SD_{ij} is the standard deviation of the pairwise differences between instruments i and j, and b_i and b_j are the corresponding mean absorption values. The pairwise CV between the AE33 instruments ranged from 26 to 45%, depending on wavelength.

The relative uncertainty of each individual instrument was then calculated as Eq. (S2):

$$\mu_i = \sqrt{\frac{(CV_{ij}/100)^2+(CV_{ik}/100)^2-(CV_{jk}/100)^2}{2}}, \text{ i,j,k} \in \{1,2,3\} \quad \text{(S2)}$$

, where μ_i represents the relative uncertainty of instrument i, and CV_{ij}, CV_{ik} and CV_{jk} are the coefficients of variation calculated for the corresponding instrument pairs, with i, j, and k denoting the three AE33 instruments. The relative uncertainty of each instrument was estimated assuming independent relative errors resulting in values of 18–32% depending on instrument and wavelength. These relative uncertainties were subsequently converted to absolute uncertainties by multiplying each relative uncertainty by the corresponding mean absorption measurement and were propagated to the incremental size-fraction absorption using Eqs. (S3) and (S4):

$$U_{PM_{1-2.5}} = \sqrt{U_{PM_1}^2 + U_{PM_{2.5}}^2} \quad \text{(S3)}$$

$$U_{PM_{2.5-7.2}} = \sqrt{U_{PM_{2.5}}^2 + U_{PM_{7.2}}^2} \quad \text{(S4)} \quad .$$

The resulting propagated uncertainties for $PM_{1\text{-}2.5}$ absorption ranged from 1.35 to 3.43 Mm^{-1}, while those for $PM_{2.5\text{-}7.2}$ ranged from 1.40 to 2.96 Mm^{-1}, from 370 to 950 nm, respectively. These values were comparable to the standard deviations of the corresponding pairwise differences observed during the instrument intercomparison, which ranged from 1.36–3.43 Mm^{-1} (AE33_2–AE33_1), 1.67–3.45 Mm^{-1} (AE33_3–AE33_1), and 1.39–2.96 Mm^{-1} (AE33_3–AE33_2).

Because the incremental absorption was obtained by subtracting two relatively small absorption signals, negative values can occur when the difference is comparable to the measurement uncertainty. Negative incremental values were observed for 21.6–35.2% of the $PM_{1\text{-}2.5}$ data and 27.4–30.9% of the $PM_{2.5\text{-}7.2}$ data, depending on wavelength. Importantly, 94.4–97.3% of the negative $PM_{1\text{-}2.5}$ values and 86.2–88.7% of the negative $PM_{2.5\text{-}7.2}$ values were within the corresponding propagated measurement uncertainty. Thus, the large majority of the negative incremental values are consistent with the estimated measurement variability and do not necessarily indicate a physically meaningful negative absorption contribution. This uncertainty assessment was therefore taken into account when interpreting the incremental coarse-mode absorption results.

S3 – Assessment of Energy-dispersive X-ray Fluorescence Measurement Uncertainty for Elemental Concentrations in $PM_{2.5}$ and PM_{10}

To assess the uncertainty relative to the measured concentrations, the absolute uncertainty of each measured element $u\ (C_{element})$ was calculated by Eq. (S5):

$$u\ (C_{element}) = \sqrt{\frac{{s_{element}}^2}{n_{samples}} + \frac{{s_{blank}}^2}{n_{blanks}}} \quad \text{(S5)}$$

, where $C_{element}$ is the blank-subtracted concentration of each element, $s_{element}$ is the standard deviation of the measured concentrations of the element across the samples, $n_{samples}$ is the number of sample replicates (3), s_{blank} is the standard deviation of the blank measurements, and n_{blanks} is the number of blank measurements (66 in total). The relative standard uncertainty $u_r\ (C_{element})$ was subsequently calculated by Eq. (S6):

$$u_r\ (C_{element}) = \frac{u\ (C_{element})}{C_{element}} \times 100. \quad \text{(S6)}$$

The uncertainty of the "Others" category was determined by combining the individual uncertainties of the elements included in this category using the root-sum-of-squares approach.

This provides a measure of the uncertainty in relation to the magnitude of the measured concentration and allows comparison of measurement uncertainty between elements and samples with different concentration levels. For the individual elements included in $PM_{2.5}$ analysis, relative uncertainties were generally low. The median was ~0.6%, compared with a higher mean of ~1.4% and standard deviation (SD) of ~3.9%, indicating that the extreme uncertainties were relatively rare. Mean element-specific relative uncertainties were generally lowest for S (~0.1%), Si (~0.4%), and Al (~0.5%), and K (~0.5%), while Zn (~0.7%), Na (~0.8%), Fe (~1.1%), and Ca (~1.4%) showed slightly higher but still generally low variability. Greater variability was observed for Mg (~2.4%), Ti (~2.9%), and Cl (~5.3%). The largest individual uncertainties reached 64.7% for Cl, 47.6% for Ti, and 19.9% for Mg. The "others" category also had high uncertainties, reaching 246.6% (mean of 26.1%). However, these extreme values were uncommon and mostly related to very low concentrations.

For PM_{10}, relative uncertainties were also generally low for the major elements. Overall, the mean was approximately 0.5% (median ~0.2%) and SD of approximately 2.6%, indicating that the highest uncertainties were relatively uncommon. Element-specific mean uncertainties were generally lowest for S (~0.1%) and Al (~0.2%), as well as for Na, K, Ca, and Fe (~0.3%). On the other hand, Mg (~0.5%), Si (~0.5%), Ti (~1.0%), Cl (~1.0%), and Zn (~1.2%) showed slightly higher but still generally low variability. The largest individual uncertainties were observed for Zn (~79.3%), Si (~21.0%), and "others" (~85.4%), while all remaining elements showed uncertainties below 10 %. As observed for $PM_{2.5}$, these extreme values were uncommon and associated with very low concentrations.